**Retrieval of dominant methane (CH4) emission sources, the first high resolution**

**(1-2m) dataset of storage tanks of China in 2000-2021**

Fang Chen[1, 2, 3, †], Lei Wang [1, 2, 4, †], Yu Wang[5, 6, *], Haiying Zhang[1, 2], Ning Wang[7],

Pengfei Ma[5, 6], Bo Yu [1, 2, 4, *]

[1]International Research Center of Big Data for Sustainable Development Goals, Beijing, 100094, China

[2]Key Laboratory of Digital Earth Science, Aerospace Information Research Institute, Chinese Academy of Sciences, Beijing, 100094, China

[3] University of Chinese Academy of Sciences, Beijing, 100049, China

[4] School of Computer Science and Information Security, Guilin University of Electronic Technology, Guilin, 541004, China

[5] State Environmental Protection Key Laboratory of Satellite Remote Sensing, Beijing 100094, China;

[6] Satellite Application Center for Ecology and Environment, Ministry of Ecology and Environment, Beijing 100094, China；

[7]College of Urban and Environmental Sciences, Peking University, Beijing, 100871, China

† These authors contributed equally to this work and should be considered as co-first authors

*Corresponding author: Yu Wang (chenfang_group@163.com), Bo Yu (yubo@radi.ac.cn)

**Abstract.** Methane (CH4) is a significant greenhouse gas in exacerbating climate change. Approximately 25% of CH4 is emitted from storage tanks. It is crucial to spatially explore the CH4 emission patterns from storage tanks for efficient strategy proposals to mitigate climate change. However, due to the lack of publicly accessible storage tank locations and distributions, it is difficult to ascertain the CH4 emission spatial pattern over a large-scale area. To address this problem, we generated a storage tank dataset (STD) by implementing a deep learning model with manual refinement based on 4,403 high spatial resolution images (1-2m) from the GaoFen-1, GaoFen-2, GaoFen-6, and Ziyuan-3 satellites over ~~cities~~city regions in China with officially reported numerous storage tanks in 2021. STD is the first storage tank dataset over 92 typical ~~cities~~city regions in China. The dataset can be accessed at https://zenodo.org/records/10514151 (Chen et al., 2024). It provides a detailed georeferenced inventory of 14,461 storage tanks, wherein each storage tank is validated and assigned the construction year (2000-2021) by visual interpretation referring to the collected high spatial resolution images, historical high spatial resolution images of Google Earth, and field survey. The inventory comprises storage tanks having various distribution patterns in different ~~cities~~city regions. Spatial consistency analysis with CH4 emission product shows good agreement with storage tank distributions. The intensive construction of storage tanks significantly induces CH4 emissions from 2005

42  to 2020, underscoring the need for more robust measures to curb $CH_4$ release and aid
43  in climate change mitigation efforts. Our proposed dataset STD will foster the accurate
44  estimation of $CH_4$ released from storage tanks for $CH_4$ control and reduction and ensure
45  more efficient treatment strategies are proposed to better understand the impact of
46  storage tanks on the environment, ecology, and human settlements.
47

48  **1. Introduction**

49      The Industrial Revolution witnessed a continuous increase in greenhouse gases,
50  resulting in global climate warming (Zhang et al., 2021). Methane ($CH_4$) is the second
51  dominant anthropogenic greenhouse gas to global climate warming with a contribution
52  of 20% (Kirschke et al., 2013) after carbon dioxide ($CO_2$). Meanwhile, $CH_4$ is more
53  effective in trapping heat, with 85 times more climate warming potency than $CO_2$ for a
54  decade or two (Stocker, 2014). The atmospheric lifetime of $CH_4$ is approximately 10
55  years, which is shorter than most other greenhouse gases; thus, reducing $CH_4$ emissions
56  is more cost-effective in lowering the climate warming potential impact (Lin et al., 2021;
57  Montzka et al., 2011). $CH_4$ is emitted mainly from energy-related activities and
58  petrochemical processes (Ding et al., 2017; Fan et al., 2023). Storage tanks,  defined
59  as large containers of crude oil or other petroleum, and industrial materials, such as
60  alcohols, gases, or liquids, are among the most significant sources of emitting $CH_4$ (Im
61  et al., 2022; Johnson et al., 2022). Without an adequate control or management strategy,
62  large amounts of $CH_4$ will escape into the atmosphere (Im et al., 2022). From a
63  greenhouse gas control standpoint, it is of great interest to examine the distribution
64  patterns of the storage tanks. With a detailed and comprehensive storage tank inventory,
65  we can effectively estimate the spatial pattern of $CH_4$ emissions and reduce the risk of
66  $CH_4$ emission by installing recovery units (Johnson et al., 2022) to promote sustainable
67  development goals. However, it is challenging to access detailed distribution records
68  for storage tanks from the public records in China.
69      Given the advances in remotely sensed technology (Chen et al., 2023; Yu et al.,
70  2023a; Yu et al., 2023b), the ready availability of high spatial resolution remote sensing
71  images via the GaoFen series satellites and the Ziyuan-3 satellite provides means to
72  extract remote sensing data for large-scale storage tanks. Numerous studies on the use
73  of automatic methods to extract storage tanks from high spatial resolution remote
74  sensing images have been performed (Fan et al., 2023; Wu et al., 2022; Yu et al., 2021),
75  including the Hough transform (Yuen et al., 1990), image saliency enhancement (Zhang
76  and Liu, 2019), support vector machines (Xia et al., 2018), and Res2-Unet+ deep
77  convolution networks (Yu et al., 2021). The focus of the works above is primarily
78  spatially limited, and the images collected for extraction are mostly pre-subtracted from
79  regions known to contain storage tanks. The transferability and the practical
80  applicability of the proposed methods remain to be clarified. To our knowledge, there
81  are limited publicly available datasets on storage tanks. Northeast Petroleum
82  University–Oil Well Object Detection Version 1.0 (NEPU–OWOD V1.0) covers 1,192
83  oil storage tanks within Daqing City (Wang et al., 2021). This dataset covers the
84  boundary boxes for each storage tank but lacks details on the storage tank inventory.
85  Another two datasets, the Oil and Gas Tank Dataset (Rabbi et al., 2020) and the Oil

Storage Tank Dataset (~~Heyer~~Airbusgeo, 2019) acquired via the Kaggle platform, have been released without georeferenced information and lack detail regarding the contour shapes. The datasets are generally proposed to improve the performance of algorithms in storage tank extraction. Currently, most studies are concentrated on algorithm development for storage tank extraction rather than exploring the spatial distribution of storage tanks in large-scale areas and the impact of storage tank construction on $CH_4$ emission in different areas over the years. The spatial distributions of storage tanks in China have not yet been investigated and recorded. The lack of storage tank datasets makes it impossible to estimate the impact of anthropogenic energy-related activities on $CH_4$ emission and air pollution.

To foster the control and reduction of $CH_4$ emissions to mitigate climate change and provide researchers with free access to detailed and georeferenced storage tank inventory to monitor the corresponding potential impact on the atmosphere and residential environment over typical ~~cities~~city regions in China, we compiled a storage tank inventory based on high spatial resolution images of the GaoFen-1, GaoFen-2, GaoFen-6, and Ziyuan-3 satellites for ~~cities~~city regions with intensive storage tanks over China. The ~~cities~~city regions are listed by the Ministry of Ecology and Environment of China with intensive storage tanks and prominent fugitive emissions, inadequate monitoring and control of treatment measures (Wang et al., 2022). There are 92 ~~cities~~city regions in total, mainly located in mid-eastern China. Given that large storage tanks may emit significant levels of $CH_4$, storage tanks ~~of size~~with footprint $\geq$ 500 m$^2$ were selected as the main target to control the reduction of $CH_4$ in the proposed inventory. To this end, we generated a complete inventory of storage tanks ~~of size~~with footprint $\geq$ 500 m$^2$ for the 92 ~~cities~~city regions in China with intensive storage tanks, which were subject to the implementation of $CH_4$ reduction measures.

In this study, firstly, we collected high spatial resolution images to cover the entire study area. We pre-processed them to synchronize the pixel intensities of ground objects in different images from different imaging sensors and study areas. Secondly, we proposed a semantic segmentation framework to construct the storage tank extraction model based on the training samples of Ningbo, Tangshan, and Dongying ~~cities~~city regions. Thirdly, the constructed model is applied to extract storage tanks in all the other ~~cities~~city regions to generate extraction results. Fourthly, the extracted storage tank result images are converted to vectors, revised and assigned the corresponding construction year by visual interpretation with reference to the historical high spatial resolution images of Google Earth, high spatial resolution images collected, and field survey. Fifthly, we explored the spatial distribution pattern of storage tanks in typical ~~cities~~city regions in China. Sixthly, we further explored the consistency of storage tank spatial patterns and $CH_4$ emission in the atmosphere and the impact of storage tank construction on time-series $CH_4$ emission change from 2005 to 2020. Finally, the uncertainties, limitations, and implications of our proposed STD dataset are discussed for studying climate change and air pollution. This new database represents the first inventory to provide a detailed distribution of the locations, boundaries of the storage tanks, and the corresponding construction year of each storage tank. The inventory documents the spatial and temporal distribution of storage tanks ~~of~~with different

sizesfootprints, and it is hoped that this work will facilitate the development of environment-friendly regulatory proposals for more effective $CH_4$ emission control and energy resource management.

## 2. Related works in mapping storage tanks

Storage tank extraction from high spatial resolution images has been of interest for many years for its significant role in storage and greenhouse gas emission. Generally, the methods for extracting storage tanks are grouped into three categories. Circle detection by Hough transformation (O'duda, 1972) and template matching (Hou et al., 2019); machine learning model construction by morphological, spectral, and textual feature engineering (Xia et al., 2018); deep learning model construction by continuous convolution operations (Fan et al., 2023). Deep learning methods have been extensively used to map storage tanks due to their strong feature learning capability and higher model transferability.

Semantic segmentation is a widely employed deep learning framework in object extraction by assigning each pixel a semantic label in the image (Chen et al., 2022; Yu et al., 2022b). Fully convolution network (FCN) (Long et al., 2015) is a basic framework of semantic segmentation with three components: backbone feature learning, convolution feature learning with skip architecture, and up-sampling layer to resample the learned feature map to the same size of the input image. Based on FCN, numerous frameworks have been inspired, such as SegNet (Badrinarayanan et al., 2017), PSPNet (Zhao et al., 2017), Unet (Ronneberger et al., 2015), DeepLabv2 (Chen et al., 2017b), and DeepLabv3 (Chen et al., 2017a). Unet has a widespread use for its easy implementation and high efficiency. The proposal of Res2-Unet+ framework for storage tank extraction (Yu et al., 2021; Zalpour et al., 2020) integrates Res2Net module (Gao et al., 2019) to Unet. Res2Net module is proposed to learn multi-scale features by learning at a more granular level. It has shown strong applicability in extracting storage tanks from images of different imaging sensors (Yu et al., 2022a). However, many storage tank pixels are still omitted due to their similar spectral characteristics with neighboring ground objects. To resist the shortage, we have proposed a new semantic segmentation framework based on Res2-Unet+ and enlarged the variability of storage tank training samples to build a more robust and accurate extraction model.

## 3. Data sources

### 3.1 Study area

The study area covers 92 typical ~~cities~~city regions (as shown in Figure 1) with intensive storage tanks over China, assigned by the Ministry of Ecology and Environment of China (Wang et al., 2022). The typical ~~cities~~city regions lack detailed monitoring and control of prominent fugitive emissions, whose effective measurements in $CH_4$ reduction emission are urgently demanding and requiring. The 92 ~~cities~~city regions tended to be located in mid-eastern China. Many of the ~~cities~~city regions are ~~located near or next to the boundary of mainland China~~coastal cities. Synthesized with a digital elevation model (DEM) from the product of the Shuttle Radar Topography Mission (SRTM) (Yang et al., 2011), we can recognize that most ~~cities~~city regions are

plains. As is acknowledged, plains are densely populated. The large population numbers will bring more frequent human activities, triggering more pollutant and greenhouse gas emissions. The lack of efficient measurements in CH$_4$ ~~reduction~~emissions will result in a more direct impact on the populations in the residential area. Therefore, exploring the spatial distribution pattern of storage tanks relative to CH$_4$ emission is significant to seek more effective solutions for CH$_4$ reduction.
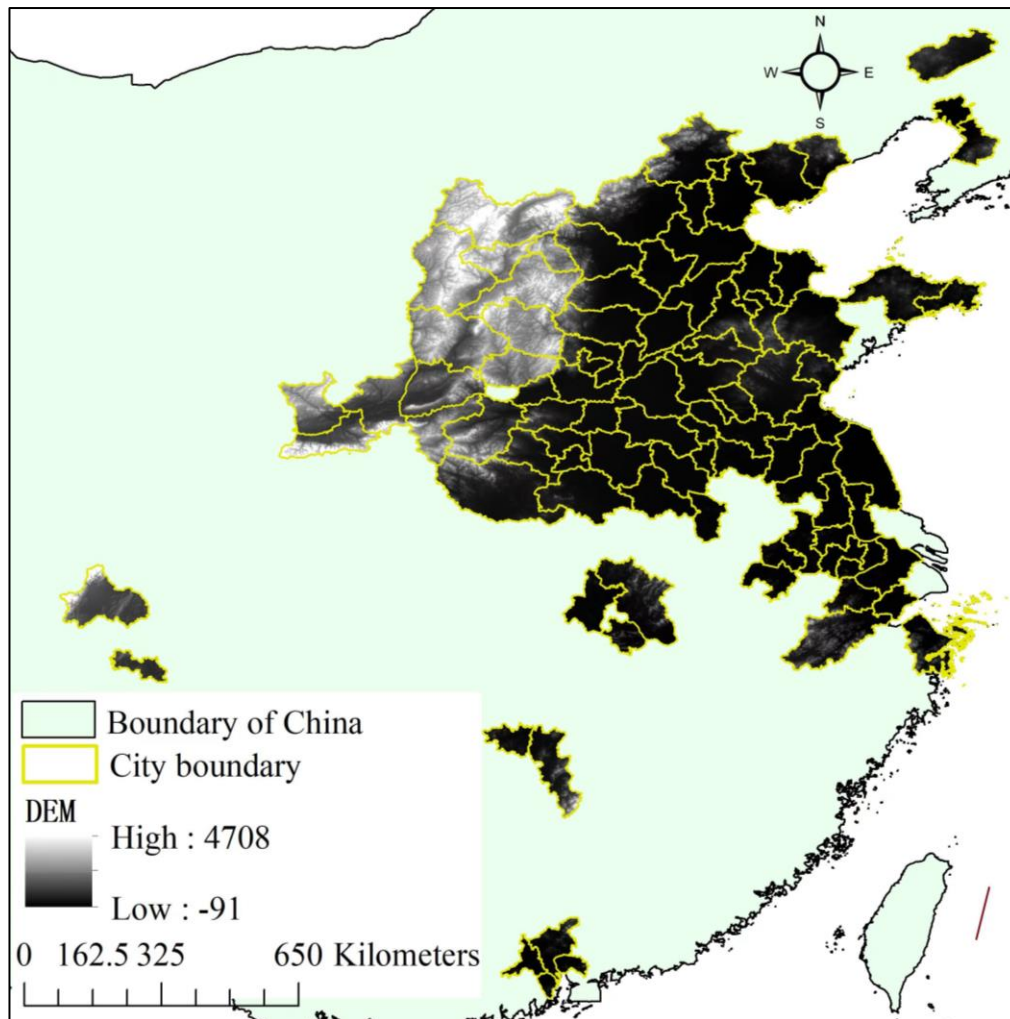


*Figure 1. Study area demonstration with digital elevation (in the unit of meter) from the Shuttle Radar Topography Mission (SRTM) product.*

## 3.2 High spatial resolution images

The high spatial resolution images used for extracting storage tanks in the 92 ~~cities~~city regions were collected from four satellites: the GaoFen-1, GaoFen-2, GaoFen-6, and Ziyuan-3 satellites in 2021. The images are collected between June and August with the least cloud coverage (<10%) from the four satellites, when different ground objects have more pronounced spectral differences, which makes it easier to distinguish storage tanks from background objects. As listed in Table 1, the images for the GaoFen-1, GaoFen-6, and Ziyuan-3 satellites have a spatial resolution of 2 m, and those for the GaoFen-2 have a spatial resolution of 1 m after fusion of the multispectral image and

the panchromatic image. Referring to Table 1, we can recognize that 4,403 images were collected. The places covered with multiple images are manually screened to one image with the best imaging quality and least cloud proportion. Based on the screened high spatial resolution images, multiple image pre-processing steps are performed to synchronize the ground objects in different images of different sensors for different study areas, comprising atmospheric correction, radiation correction, geometric precision correction, image fusion, image projection, uniform color processing, and image mosaicking.

*Table ~~II~~. Imaging characteristics of each high spatial resolution satellite and the number of collected images of different satellites covering 92 typical ~~cities~~city regions in China between June and August 2021. The notation Pan is short for Panchromatic band, and Multi represents multi-spectral band*

|  | GaoFen-1 | GaoFen-2 | GaoFen-6 | Ziyuan-3 | Total |
|---|---|---|---|---|---|
| **Spatial resolution** | 2m(Pan)/ 8m(Multi) | 1m(Pan)/ 4m(Multi) | 2m(Pan)/ 8m(Multi) | 2m(Pan)/ 6m(Multi) |  |
| **Multi-spectral Band** | Red/Green/ Blue/Near-Infrared | Red/Green/ Blue/Near-Infrared | Red/Green/ Blue/Near-Infrared | Red/Green/ Blue/Near-Infrared |  |
| **Number** | 1,289 | 1,330 | 139 | 1,645 | 4,403 |

## 3.3 Land use land cover product

Given that storage tanks are constructed mainly in ~~residential areas~~urban area due to the high expense of transportation of pipelines, a 10 m land use land cover (LULC) product of the Esri Land Cover in 2021 (Karra et al., 2021) is used for subtracting the study area to minimize the impact of complex background objects in the high spatial resolution images following the workflow as shown in Figure 2. The land use product of the Esri Land Cover is generated based on the Sentinel-2 images from the European Space Agency (ESA) with an overall accuracy of 75% (Venter et al., 2022), which has been updated every year since 2017. It comprises nine ground object categories: water, trees, flooded vegetation, bare ground, crops, snow/ice, clouds, rangeland, and built area. Since storage tanks are mostly constructed in urban areas, the categories of built area and bare ground are recognized as potential areas for constructing storage tanks. Consequently, the corresponding ground object category products of built area and bare ground are subtracted from the LULC product 2021 and used to mask the high spatial resolution images of the 92 ~~cities~~city regions, as demonstrated in Figure 2. Pixels locating outside the mask area in the high spatial resolution images, whose intensities are assigned zero. The masked high spatial resolution images of the 92 ~~cities~~city regions are further used for storage tank extraction.
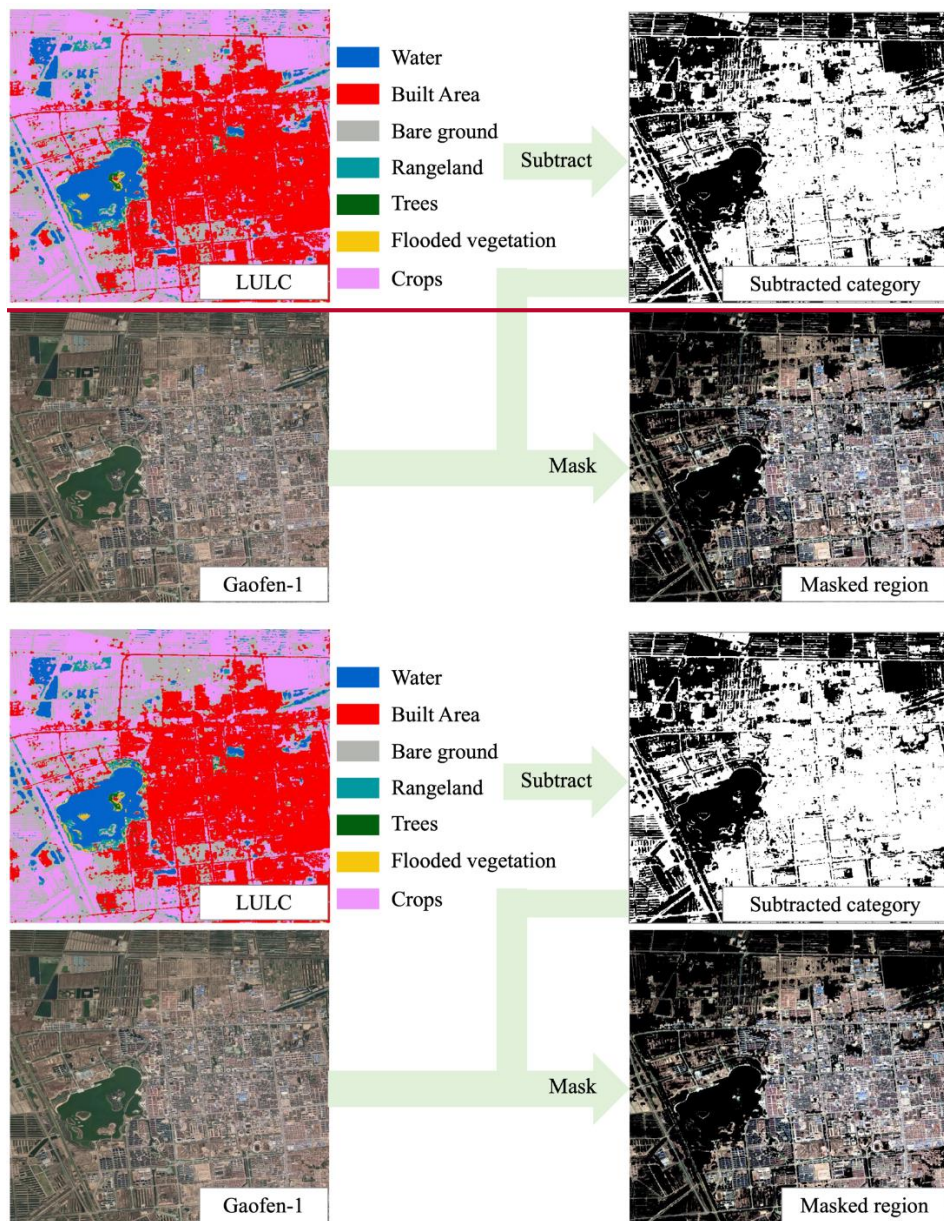
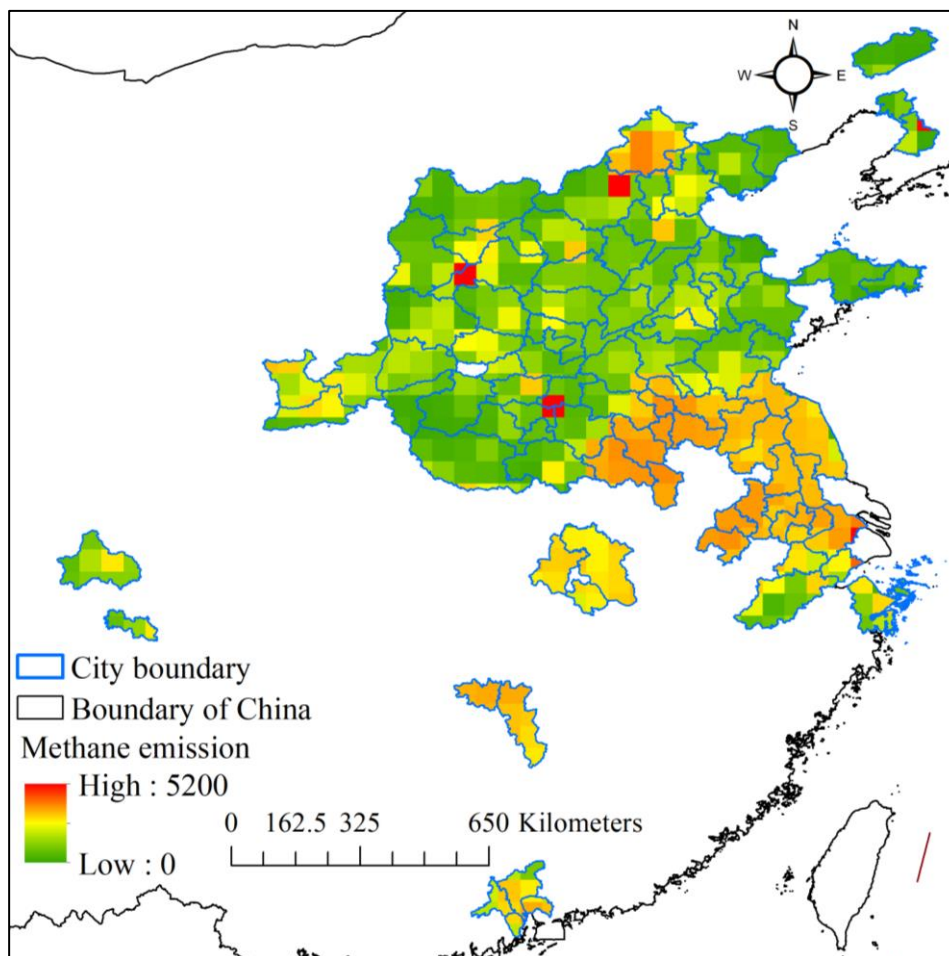*Figure 2. Subtraction of potential area with storage tanks from high spatial resolution images.*

## 3.4 CH$_4$ product image

As storage tanks are a dominant source of CH$_4$ emission, we have collected CH$_4$ emission products to explore the spatial consistency of CH$_4$ with the density of storage tanks and the impact of storage tank construction over time on CH$_4$ emission. There have been many CH$_4$ emission product images proposed, including the Community Emission Data System (CEDS) (Hoesly et al., 2018), the product from Peking University (Peng et al., 2016), the Emissions Database for Global Atmospheric Research (EDGAR) (Crippa et al., 2019), the Regional Emission Inventory in Asia (REAS) (Kurokawa et al., 2013), and Greenhouse Gas and Air Pollution Interactions and Synergies (GAINS and ECLIPSE) (Amann et al., 2011). Since our collected high spatial resolution remote sensing images were taken in the year 2021, the spatial

241　consistency and the impact of storage tank construction on CH₄ emission are explored
242　using the CH₄ emission product of GAINS, which offers a comprehensive series of data
243　accessible to the public (Lin et al., 2021). The dataset of GAINS was selected over the
244　other four products because the four products lacked continuous updates with limited
245　temporal coverage until 2015.
246　　　We adopted the estimated CH₄ emission from energetic activities product of the
247　ECLIPSE V6b Baseline scenario from GAINS. It is a global annual product with a
248　spatial resolution of 0.5° and a temporal coverage of 1990-2050 at an interval of 5 years.
249　For the estimated CH₄ emission from GAINS in the years 1990-2018, the product is
250　generated from statistics of the International Energy Agency (IEA), and the years 2019-
251　2050 are from the outlook of the IEA World Energy Outlook (Lane, 2018). To
252　synchronize with the temporal scope of storage tank construction from 2000 to 2021,
253　the CH₄ emission products of 2005, 2010, 2015, and 2020 are collected.
254　　　As demonstrated in Figure 3, the emission of CH₄ in 2020 varies remarkably in
255　different areas. There are many clusters of CH₄ emission in the study area, with the
256　highest of 5,160.62 Tg CH₄ yr⁻¹. CH₄ in the atmosphere of ~~cities~~city regions located in
257　southeastern China is generally higher than that of ~~cities~~city regions in northwestern
258　China in 2020.



*Figure 3. Demonstration of CH₄ distribution from energetic activities over the study area in the year 2020.*

## 4. Methodology

As depicted in Figure 4, the workflow of generating a storage tank dataset consists of three sections: harmonizing the pixel intensities of different ground objects across high spatial resolution images captured by different sensors in different study areas; producing a storage tank dataset by constructing a storage tank extraction model based on the harmonized high spatial resolution images; assigning the construction year of each storage tank by multiple experts through visual interpretation referring to the historical high spatial resolution images from Google Earth, high spatial resolution images collected, and filed survey from Google Earth.
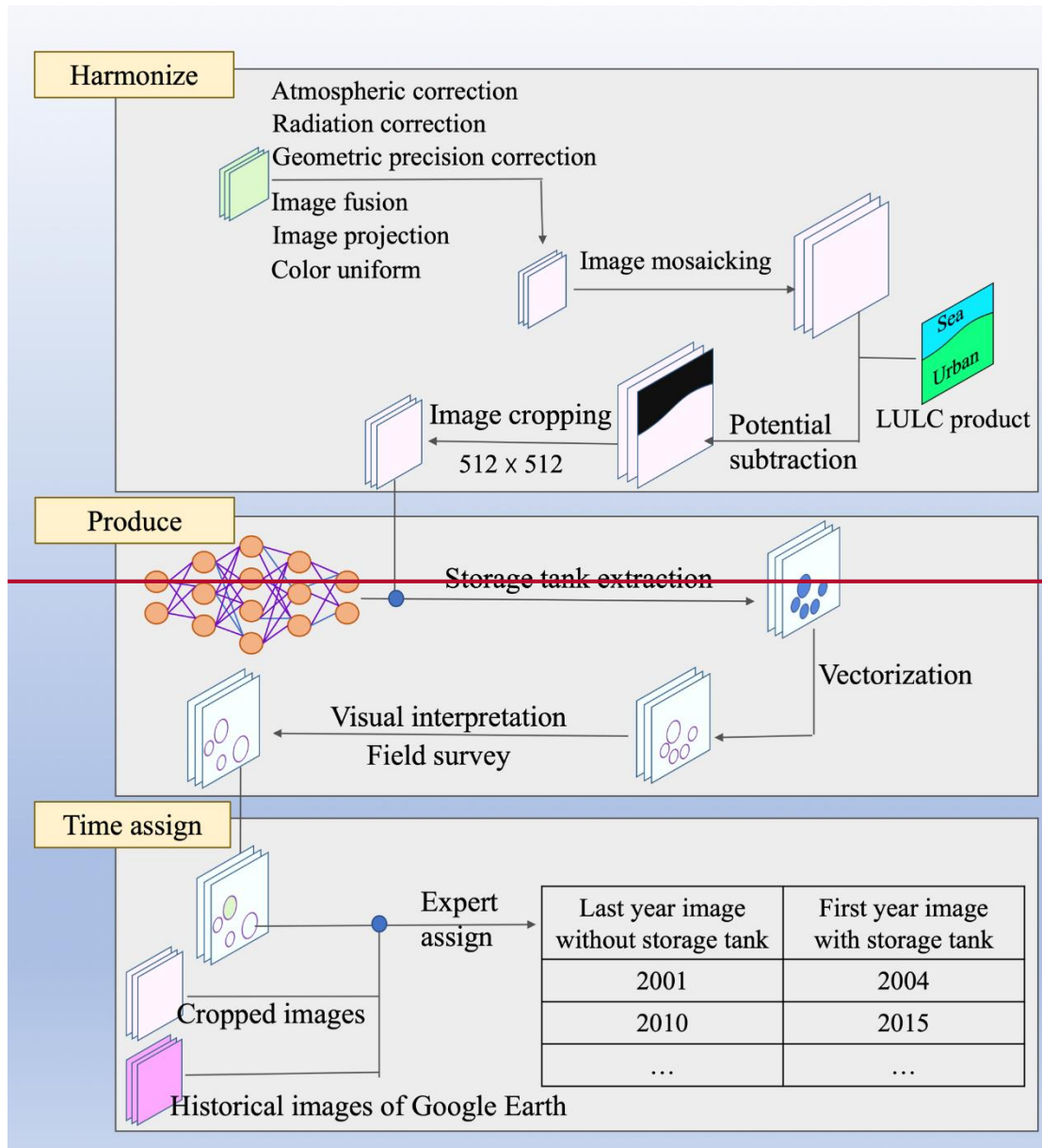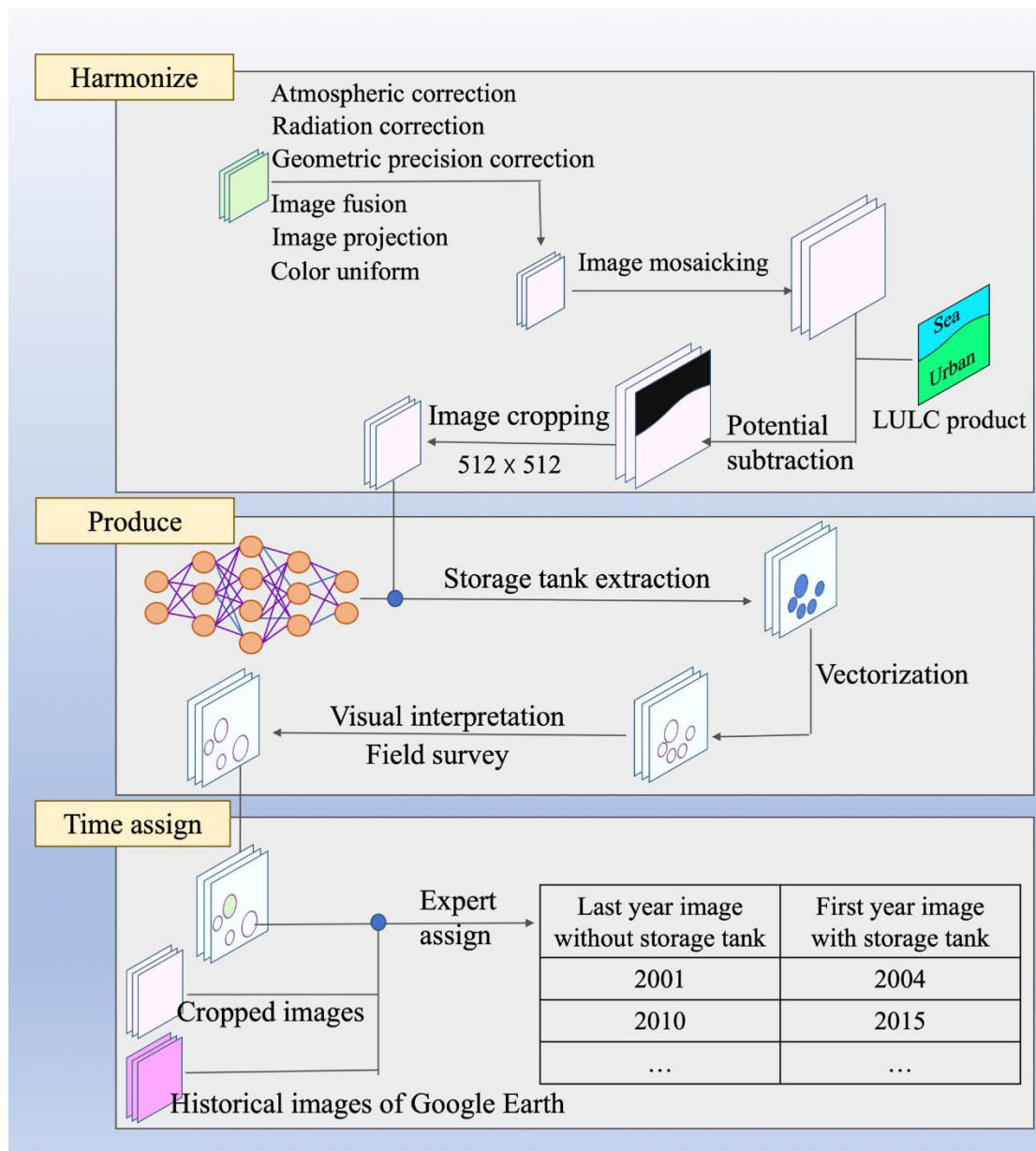
*Figure 4. Flow chart for storage tank inventory production.*

## 4.1 Image harmonizing

Pixel intensities for ground objects are standardized to ensure consistency across the high spatial resolution images collected. This harmonization process mitigates the effects of atmospheric variations and discrepancies between imaging sensors captured at different times. The standardization includes atmospheric correction, radiometric calibration, geometric alignment, image fusion, reprojection, and color normalization. In terms of atmospheric correction, the widely used radiation transfer model of the second simulation of the satellite signal in the solar spectrum (6S) (Vermote et al., 1997) is adopted to determine the atmospheric correction coefficient and eliminate the absorption and scattering impact of atmospheric molecules and aerosols for all the collected high spatial resolution images. The strategy of local histogram matching

(Shen, 2007) is used to correct radiation differences of the same ground object category in different high spatial resolution images. To improve the geometric precision of the high spatial resolution images collected, we automatically generated 1000 ground control points by a widely used key point detector of scale-invariant feature transform (SIFT) for each city. We calculated the parameters for affine transformation with reference to the world imagery of Environmental Systems Research Institute (ESRI) (Hou et al., 2021). Pixel-wise image fusion is conducted on images collected from each high spatial resolution satellite since they consist of multispectral images with a coarser spatial resolution than the panchromatic image, as demonstrated in Table 1. To optimize the utilization of the gathered images, we leveraged the wavelet transform (Sahu and Sahu, 2014) for the automatic fusion of multispectral and panchromatic images. To address discrepancies in the projections of the varied high-resolution images we collected, we standardized all the images to the Universal Transverse Mercator (UTM) projection using bilinear interpolation for consistency. To maintain visual consistency across images from different sensors or regions, it is crucial to standardize the color representation of identical ground objects. In this study, we implemented a nonlinear stretching technique to modify pixel intensity distribution. This was accomplished by constructing a color look-up table (Majumder et al., 2000) to ensure uniformity in spectral intensities across the various images.

The harmonized high spatial resolution images were further mosaicked to large image patches to integrate overlapping areas from adjacent high-resolution images, ensuring comprehensive coverage and continuity of the observed regions. Referring to the LULC product of the Esri Land Cover product in 2021, the mosaicked image patches were subtracted with the ground object category of built area and bare ground, identified as potential areas with storage tank constructions. Finally, for storage tank extraction, the subtracted images were cropped to a size of 512×512 pixels, a size compatible with the computational limits of our GPU hardware.

**4.2 Production of storage tank dataset**

**4.2.1 Proposed framework for storage tank extraction**

Stemming from the recently developed semantic segmentation framework for storage tank extraction, Res2-Unet+ ~~by Yu et al.~~ (Yu et al., 2021), we proposed a new network structure Res2-UnetA to build storage tank extraction model. As shown in Figure 5A, our proposed framework integrates the Res2Net module (Figure 5B) and channel-spatial attention module (Figure 5C) to enhance the significant features for multi-scale storage tank extraction. During the process of feature map down-scaling, the Res2Net module can learn the multi-scale features from multiple sub-networks and concatenate the multi-scale features to enlarge the visual perception capability. In the stage of feature map up-sampling, our proposed channel-spatial attention module adopted after each feature map concatenation operation can increase the feature learning efficiency and enlarge the feature learning scale by synthesizing channel-wise and spatial attention feature learning modules. Detailed calculation of channel-wise and spatial attention modules can be referred to Equations (1)-(7).
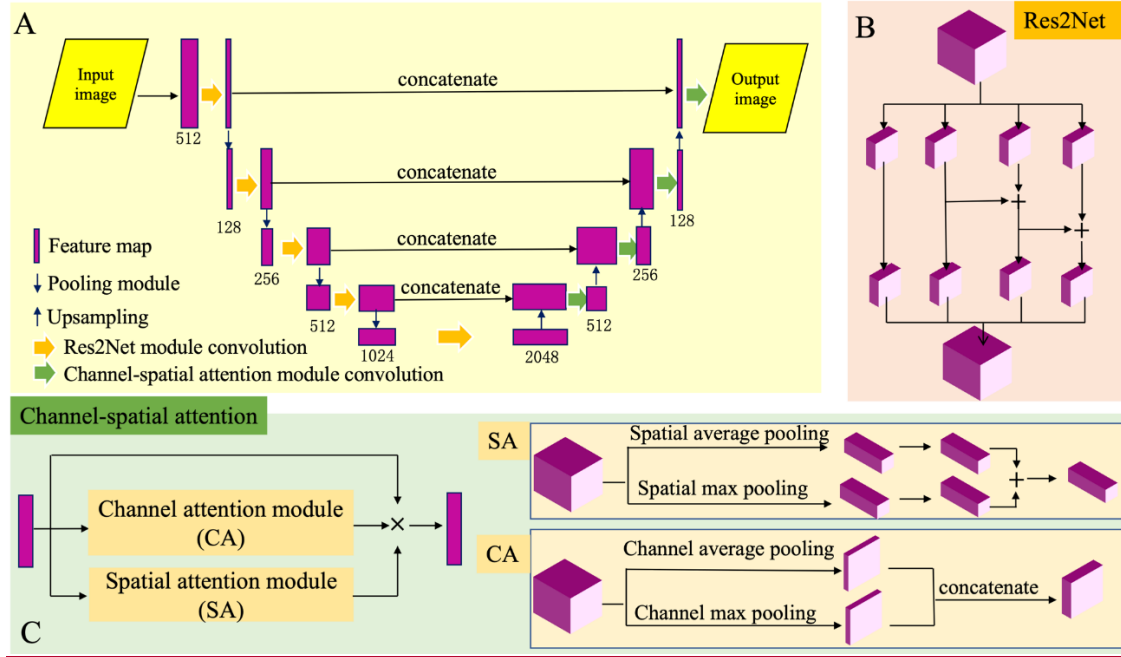
Figure 5. Network structure of our proposed Res2-UnetA: (A) network general demonstration; (B) structure of Res2Net module; (C) structure of channel-spatial attention module.

$$sa_f = \frac{\sum_{i=0}^{m}\sum_{j=0}^{n} f_{i,j}}{m \times n} \tag{1}$$

$$sm_f = \max(f_{i=0,\cdots,m,\,j=0,\cdots,n}) \tag{2}$$

$$ca_f = \frac{\sum_{c=0}^{h} f_{c=k}}{h} \tag{3}$$

$$cm_f = \max(f_{c=0,\cdots,h}) \tag{4}$$

$$SA(f) = conv(conv(sa_f) + conv(sm_f)) \tag{5}$$

$$CA(f) = conv(concatenate(ca_f, cm_f)) \tag{6}$$

$$CSA(f) = f \times CA(f) \times SA(f) \tag{7}$$

Spatial average pooling (sa) and spatial maximum pooling (sm) operations are calculated as the average value and maximum value of input feature map f with size of m×n, as described in Equations (1)-(2). Correspondingly, the channel-wise average (ca) and maximum pooling (cm) operations are the average feature values of all the h channels and the maximum feature values of all the channels in Equations (3)-(4). The output feature map of the spatial attention module (SA) and channel attention module (CA) are calculated according to Equations (5)-(6), respectively, and the synthesis of

the feature maps from the channel and spatial attention modules is organized by multiplication, as illustrated in Equation (7). Through multi-scale feature enhancement by our proposed Res2-UnetA framework, it can learn the multi-scale storage tank features hierarchically and comprehensively from the high spatial resolution images of the different imaging sensors.



Figure 5. Network structure of our proposed Res2-UnetA: (A) network general demonstration; (B) structure of Res2Net module; (C) structure of channel-spatial attention module.

$$sa_f = \frac{\sum_{i=0}^{m}\sum_{j=0}^{n} f_{i,j}}{m \times n} \tag{1}$$

$$sm_f = \max(f_{i=0,\cdots,m,\, j=0,\cdots,n}) \tag{2}$$

$$ca_f = \frac{\sum_{c=0}^{h} f_{c=k}}{h} \tag{3}$$

$$cm_f = \max(f_{c=0,\cdots,h}) \tag{4}$$

$$SA(f) = conv(conv(sa_f) + conv(sm_f)) \tag{5}$$

$$CA(f) = conv(concatenate(ca_f, cm_f)) \tag{6}$$

$$CSA(f) = f \times CA(f) \times SA(f) \tag{7}$$

**4.2.2 Storage tank model construction and dataset generation**

Based on our proposed framework Res2-UnetA, the pre-processed high spatial resolution images for the ~~cities~~city regions of Ningbo, Tangshan, and Dongying are used to train the storage tank extraction model. Ningbo, Tangshan, and Dongying are three typical ~~cities~~city regions in China with large densities of storage tanks so that they

13

can provide large quantities of training samples with high spectral and textual feature variety in different sizes. The storage tanks for the training dataset are interpreted visually by three experts in a relative field referring to the collected high spatial resolution images. The model is finetuned based on the optimized model from Res2-Unet+ ~~by Yu et al.~~ (Yu et al., 2021) with a learning rate of 0.01. It converges to the optimum at the iteration of 69.

With the optimized model, the storage tanks for the remaining ~~cities~~city regions are extracted accordingly and vectorized to the shapefile. While the enhanced model for extracting storage tanks generally performs well, it's not infallible. Some tanks are inadvertently missed, and other objects with similar spectral or textural characteristics are occasionally mistakenly identified as tanks. Therefore, ~~the~~each vectorized shapefile is further refined manually by visual interpretation with referral to the high spatial resolution images. Due to the inconsistent spectral intensities for the storage tanks in the images, triggered by shadows and different viewing angles, the vectorized storage tanks in the inventory take different shapes. To synchronize the storage tanks in the inventory taking on a round shape, we re-construct a circle for each extracted storage tank according to the radius calculated in the inventory, and the inventory is updated with the re-constructed circle. To facilitate the dating of each storage tank's construction year, the reconstructed circle for each extracted storage tank has been manually validated and refined by six experienced experts through visual interpretation based on our collected high spatial resolution images and field survey.

**4.3 Construction year assignment**

In the STD dataset we developed, a team of six experts determines the construction year for each storage tank by conducting visual assessments using high-resolution historical images available on Google Earth, with the cutoff date for this process being January 1$^{st}$, 2024. The intermittent availability of historical high-resolution images on Google Earth poses a challenge in determining the precise construction years for many storage tanks, especially when images from successive years are missing. We documented the most recent year when a storage tank was absent (last year image without storage tank) and the earliest year when it was first observed (first year image with storage tank) in the historical imagery, as illustrated in Figure 4. The actual construction year lies within this timeframe. For analysis simplicity, we've designated each tank's initial observed year as the construction year.

Since the high-resolution images used to compile the storage tank dataset were captured in 2021, it is presumed that all tanks were constructed no later than this year. However, due to the absence of updated high-resolution imagery on Google Earth, 488 tanks remain undetected in the historical records. For these, the year of construction has been inferred as 2021, following thorough visual confirmation using the high-resolution images we have acquired. The considerable lapses in historical high-resolution imagery on Google Earth necessitate assigning a provisional construction year 2021 to 630 storage tanks. The year of 2021 marks the earliest documented evidence of these tanks' existence in the high-resolution images we collected, beyond which no prior images are available. For the storage tanks built before 2000, they are recorded with the first year image with storage tank in the shapefile, but lacking the last year image without storage

14

tank in our proposed dataset STD due to the limited accessibility of high spatial resolution images before 2000 from Google Earth.

## 5. Results

### 5.1 Spatial distribution of storage tanks

Following the workflow in Figure 4, the storage tanks in the 92 typical ~~cities~~city regions of China are extracted based on the high spatial resolution images using the trained semantic segmentation model. Given that large capacity storage tanks are known to release significant levels of $CH_4$, resulting in climate warming, the proposed inventory focuses on storage tanks with an area of no less than 500 $m^2$. 14,461 storage tanks are extracted from the 92 ~~cities~~city regions with areas ranging from 500 $m^2$ to 18,583.15 $m^2$. As shown in Figure 6, the storage tanks are distributed unevenly in different ~~cities~~city regions and reflect different ~~sizes~~footprints and spatial distribution patterns. To explore the different distribution patterns, the storage tanks are categorized into three groups according to the area: 500-1,000 $m^2$, 1,000-10,000 $m^2$, and ≥10,000 $m^2$. The accumulated number of storage tanks of different ~~sizes~~footprints for all the ~~cities~~city regions is compiled as shown in Figure 7. It may be seen that storage tanks of 500-1000 $m^2$ are more than those ~~of~~with larger ~~sizes~~footprints. The relatively smaller storage tanks are more widely used in industry. Due to the high cost of construction, considering all the ~~cities~~city regions, the maximum number of large storage tanks ~~of~~ ~~size~~with footprint ≥10,000 $m^2$ is found to be seven for the city of Tangshan. Notably, there are few ~~cities~~city regions with storage tanks of 10,000 $m^2$ in ~~size~~footprint.
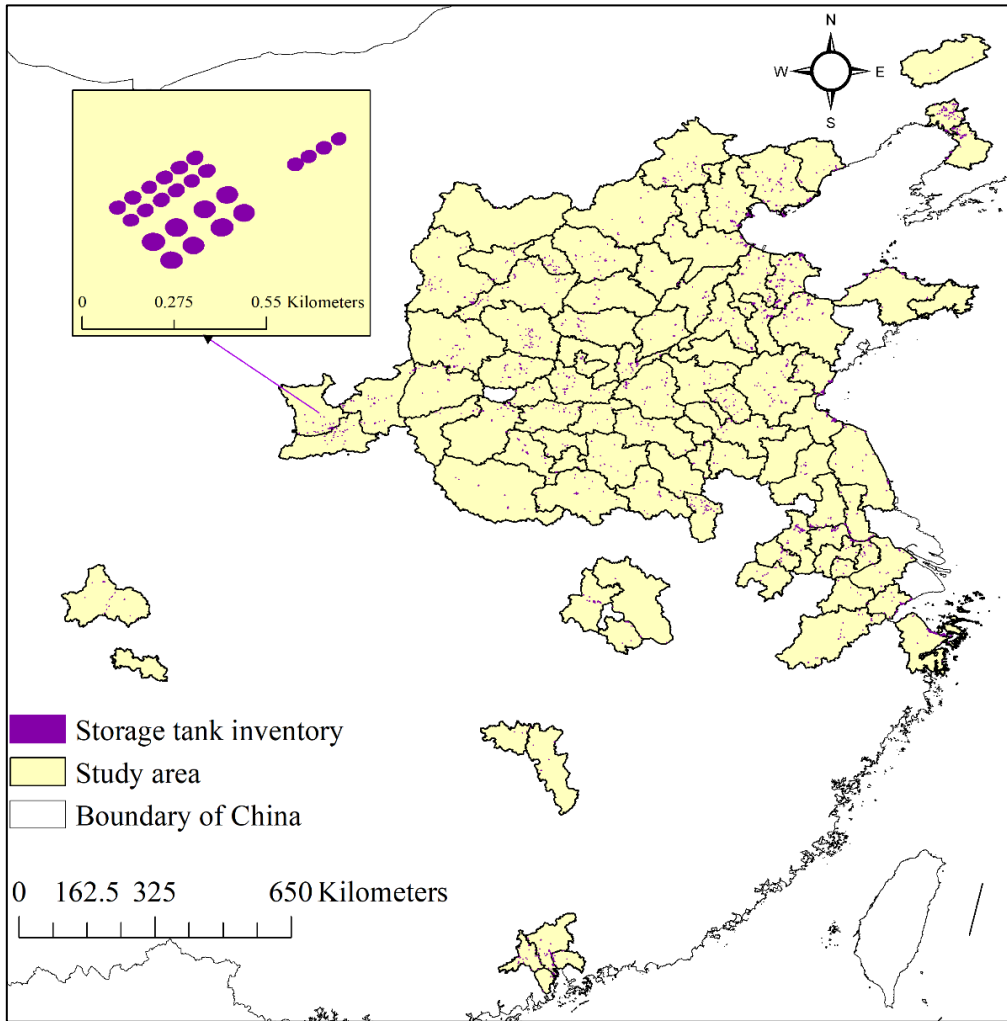
*Figure 6. Inventory for storage tanks of the 92 typical ~~cities~~city regions.*
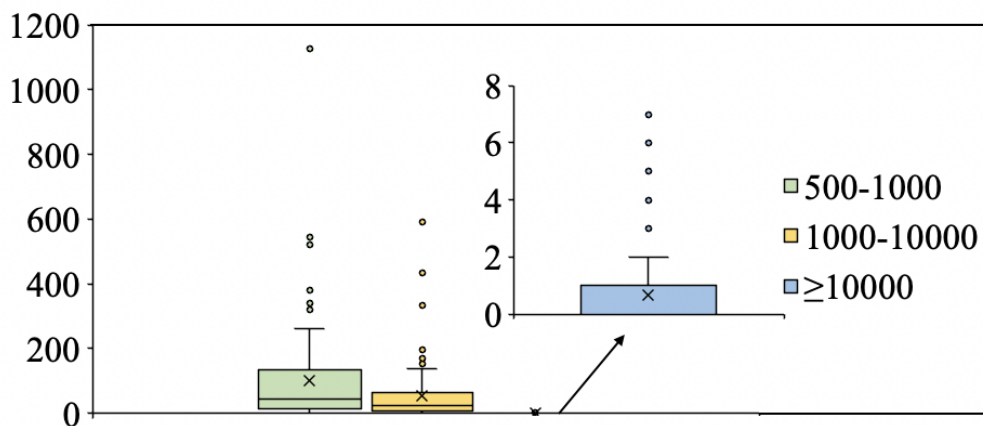


*Figure 7. Box plot of storage tank distribution for the different ~~size~~footprint*

*categories (m$^2$) for the 92 ~~cities~~city regions.*

About the 92 ~~cities~~city regions examined, 38 ~~cities~~city regions have storage tanks with an accumulated ≥100, as shown in Figure 8A. Dongying has the largest

accumulated number of 1719, about twice that of Ningbo, the second highest ranked city with 981 storage tanks. Weifang and Panjin are next in rank with storage tanks more than 500. The number of storage tanks ~~of size~~with footprint 500-1000 m² is greater than that for 1,000-10,000 m² and ≥10,000 m² for most ~~cities~~city regions. This finding indicates the widespread use of smaller storage tanks in different industries. Furthermore, there are 36 ~~cities~~city regions with an accumulated number of < 50 (Figure 8B). Among the 36 ~~cities~~city regions, Hebi is the only city with four storage tanks of ≥10,000 m² in ~~size~~footprint. The other ~~cities~~city regions, except Tangshan, do not have that large storage tanks. No storage tanks ~~of size~~with footprint ≥500 m² are observed for the ~~cities~~city regions of Taian, Weihai, and Zigong.
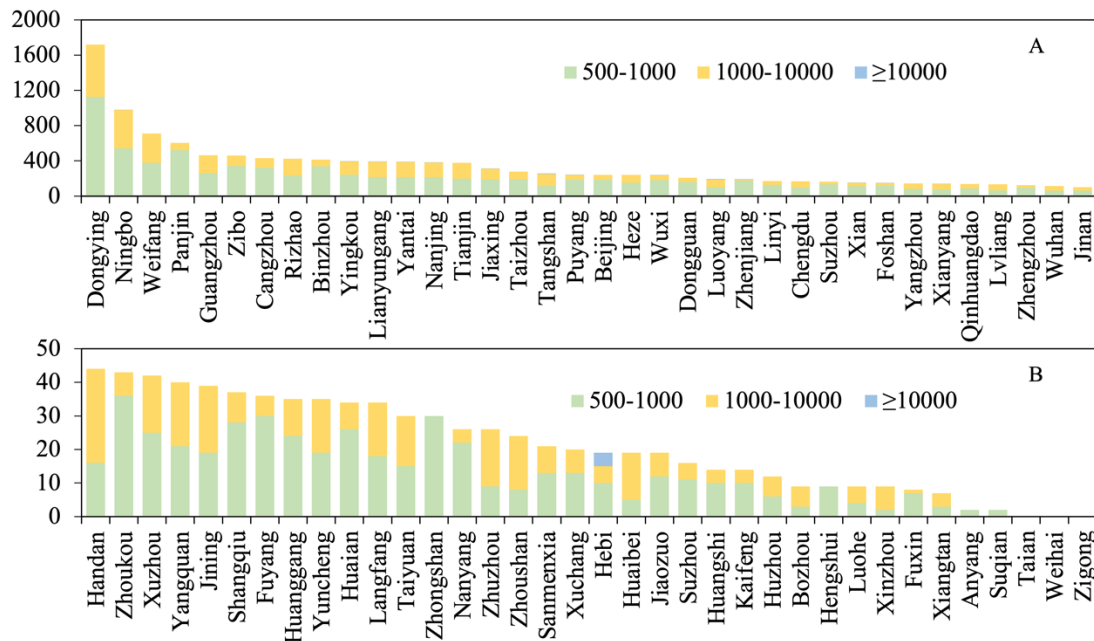


*Figure 8. Number of storage tanks of different ~~size~~footprint categories (m²) in the various ~~cities~~city regions: (A) ~~cities~~city regions with an accumulated storage tank number ≥100; (B) ~~cities~~city regions with accumulated storage tank number of <50.*
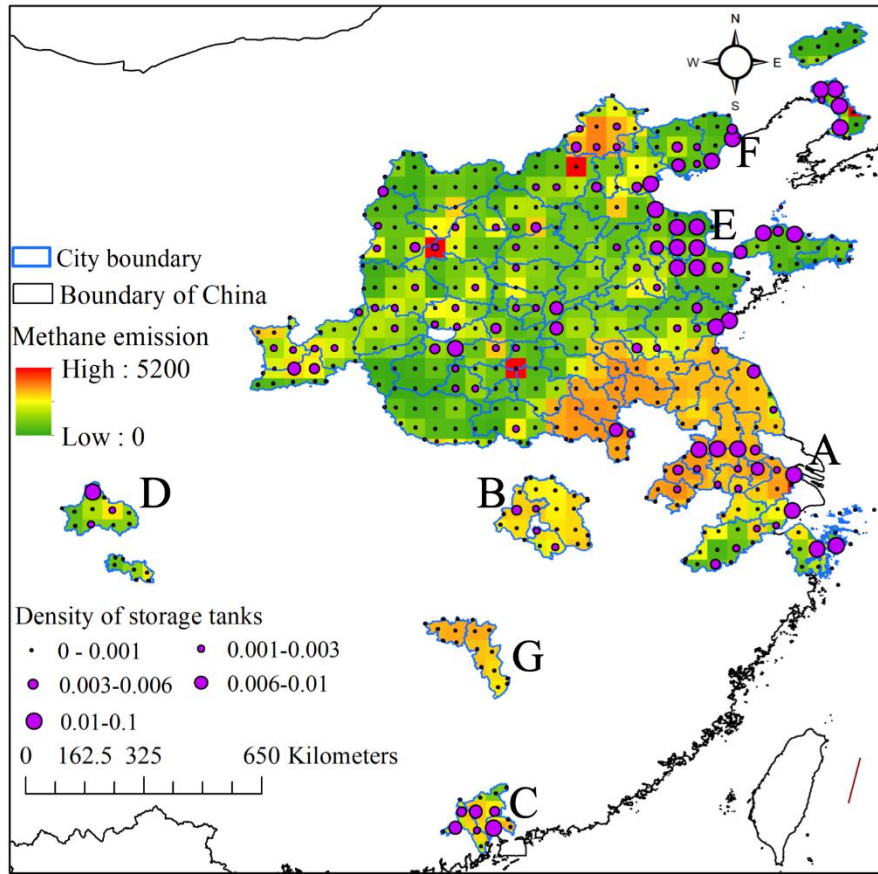
## 5.2 Spatial consistency with CH₄ emission

To explore whether the distribution patterns of storage tanks influence CH₄ emissions significantly, we explored the spatial consistency between estimated CH₄ from energy emission products in year of 2020 and the density of storage tanks in our proposed dataset STD over the study area. Given the coarser spatial resolution of the CH₄ emission product at 0.5°, which is less detailed than that of the high spatial resolution images used for generating our storage tank dataset, we've calculated storage tank density to align with each pixel grid of the CH₄ data. The density is defined by the total storage tank area ratio within each corresponding 3025 km² pixel grid area (55km × 55km), where 55 km is an approximation of 0.5° latitude or longitude at the equator.

The storage tank density is calculated for each grid pixel of the CH₄ emission product and is demonstrated in Figure 9. We can recognize that large-scale areas with high CH₄ emission in the atmosphere generally cluster large densities of storage tanks (clustered cases of A, B, C, and D). The sparsely distributed storage tanks with high

density are mostly accompanied by a higher CH$_4$ emission than the neighborhood (as shown in cases of E). There are also some ~~cities~~city regions with a high density of storage tanks and low CH$_4$ emission estimation, especially ~~at the border of mainland China~~coastal cities, as in the cases of F. That could be attributed to the coastal air currents, which will likely disperse CH$_4$ emissions more effectively. It also needs to be pointed out that for the ~~cities~~city regions marked as G in Figure 9, the estimated CH$_4$ emission is relatively high, but the density of storage tanks is low. One possible reason is the unrestrained leakage of CH$_4$ from the storage tanks, highlighting the urgent need for effective control measures. Alternatively, other high-energy activities within these regions might be significant CH$_4$ contributors, suggesting a need for comprehensive investigation into broader mitigation strategies.
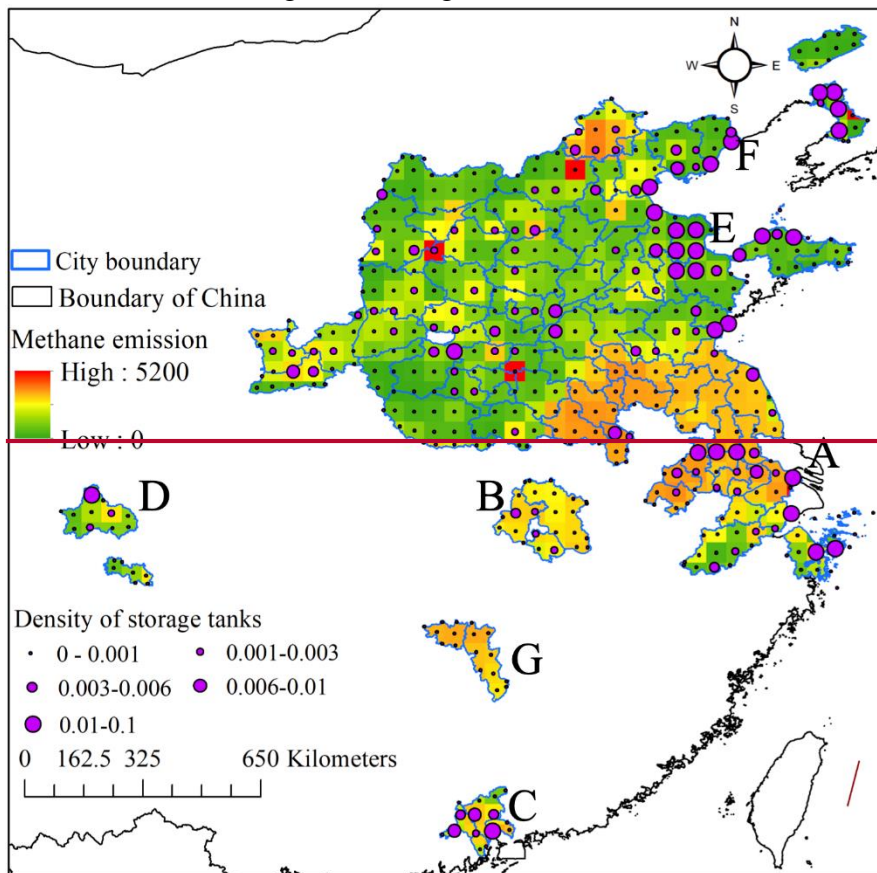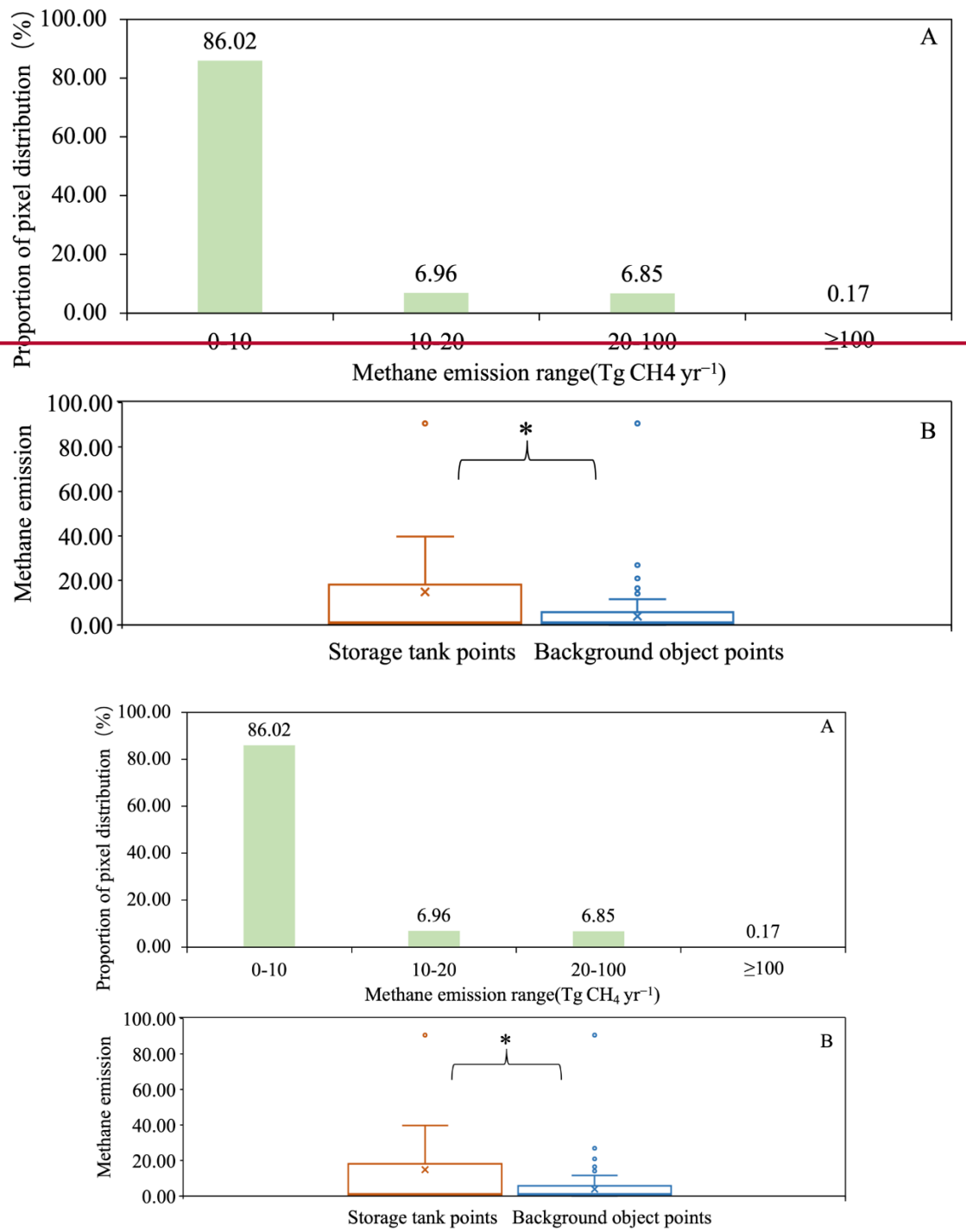
*Figure 9. Spatial distribution pattern of different densities of storage tank area with different CH₄ emissions in the atmosphere.*

To objectively explore the spatial consistency of storage tank distribution and $CH_4$ emission from energetic activities, we randomly selected 4000 storage tank pixels and 4000 background object pixels to evaluate the significance of the impact of storage tanks on $CH_4$ emission. Referring to Figure 3, the value of $CH_4$ emission varies by a large margin between 0.000055 and 5160.32 Tg $CH_4 yr^{-1}$. The large value gap of $CH_4$ emission will cause bias in the differential significance test. We generated the quantity distribution of pixels with different $CH_4$ emission value gaps (as shown in Figure 10A) and found that 99.83% of pixels have a $CH_4$ emission value of <100 ~~Tg CH₄yr~~ Tg $CH_4$ $yr^{-1}$. Therefore, the 4000 storage tank pixels and 4000 background object pixels are randomly selected from pixels with a $CH_4$ emission value of <100 ~~Tg CH₄yr~~ Tg $CH_4 yr^{-1}$. As shown in Figure 10B, the $CH_4$ emission values of storage tank pixels are statistically significantly larger than that of background object pixels ~~with~~at a confidence level of p ~~value <~~=0.05. It indicates storage tanks are significant energetic sources of $CH_4$ emission. With our proposed dataset STD, it is possible to monitor the greenhouse gas emissions from storage tanks to take effective measurements for potential climate warming reduction in time.

**A**

Proportion of pixel distribution (%)

100.00
80.00
60.00
40.00
20.00
0.00

86.02

6.96    6.85    0.17

0-10    10-20    20-100    ≥100

Methane emission range(Tg CH4 yr$^{-1}$)

**B**

Methane emission

100.00
80.00
60.00
40.00
20.00
0.00

*

Storage tank points    Background object points

*Figure 10. Distribution pattern of storage tank pixels with different CH$_4$ emission estimations: (A) Proportion of pixels with different CH$_4$ emission estimations; (B) box plot of CH$_4$ emission (Tg CH$_4$yr$^{-1}$) of storage tank points and background object points.*

## 5.3 Temporal impact on CH$_4$ emission

Given the constraints of historical high-resolution imagery on Google Earth, the earliest ascertainable construction year for storage tanks is set to 2000, with the latest capped at 2021, as depicted in Figure 11. Therefore, our dataset STD includes storage
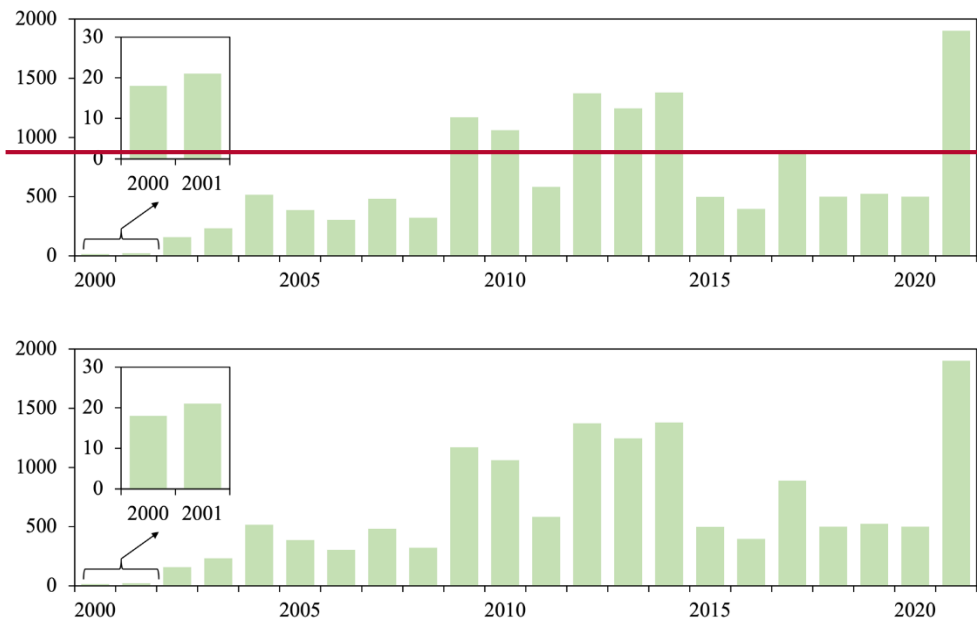
tanks constructed in years of 2000-2021. It is noted that storage tanks were largely constructed in 2009, 2010, 2012, 2013, and 2014, while those in 2000 and 2001 were less constructed, with quantities of approximately twenty. To align with the construction temporal range of storage tanks in the dataset, $CH_4$ emission products of 2005, 2010, 2015, and 2020 are utilized, as these emission products are updated every five years. To explore the impact of storage tank construction on $CH_4$ emission, the storage tanks are grouped by the product year of $CH_4$, as listed in Table II. Storage tanks built in the years 2000 and 2021 are excluded from the impact analysis due to the exceed of the corresponding impact temporal range of $CH_4$ emission.

Table II. Correspondence between the year of $CH_4$ emission product and group of construction years of storage tanks.

| Year of $CH_4$ emission product | Year group of storage tanks constructed |
|---|---|
| 2005 | 2001-2005 |
| 2010 | 2006-2010 |
| 2015 | 2011-2015 |
| 2020 | 2016-2020 |



*Figure 11. Number of storage tanks constructed in different years.*

It is noted that the spatial resolution of the $CH_4$ emission product is coarser than the images we used to generate our proposed STD dataset; similar to the works in spatial consistency exploration, the storage tanks constructed in different groups of years are gridded by the $CH_4$ emission product, and the density of storage tanks is calculated for each grid. We conducted a correlation analysis to explore the statistical significance of the impact of storage tank construction on $CH_4$ emission over 2005-2020 at levels of $p=0.05$ and $p=0.1$, respectively. Moreover, the rate of $CH_4$ emission change and ~~oil~~storage tank density newly constructed every five years are calculated according to Equation (8) and demonstrated accordingly in Figure 12.

21

$$R=(I_{2020}-I_{2005})/4 \qquad\qquad (8)$$
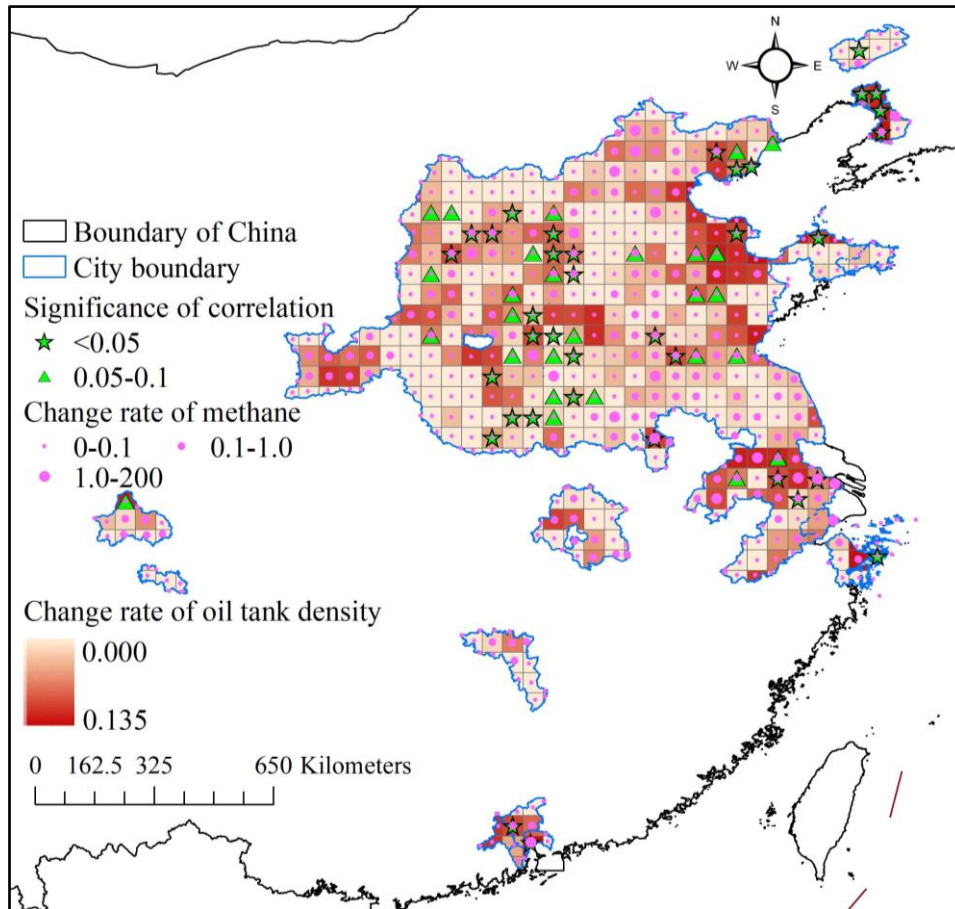


*Figure 12. Significance of correlation between change rate of ~~oil~~storage tank density and CH$_4$ emission change.*

Both CH$_4$ emission and newly constructed storage tank density increased from 2005 to 2020, with positive rates in Figure 12. Over the 92 ~~cities~~city regions in this study, storage tanks are constantly being constructed to meet the industrial demand, but CH$_4$ emission is continuously increasing too. The storage tanks of ~~cities~~city regions such as Yingkou, Panjin, Dongying, Binzhou, Yantai, Weifang, Tangshan, Linyi, Rizhao, Puyang, Xi'an, Pingdingshan, Huainan, Nanjing, Maanshan, Changzhou, Wuxi, Chengdu, Foshan, Dongguan, and Guangzhou are constructed with higher rates than the other ~~cities~~city regions. CH$_4$ from energetic activities is emitted at a highly increasing rate in multiple ~~cities~~city regions, such as Beijing, Yingkou, Zhenjiang, Nanjing, Maanshan, Changzhou, Wuxi, Shijiazhuang, Huainan, and Dongguan. Grids showing a statistically significant correlation (p<0.1) between storage tank density and CH$_4$ emissions typically display a notable rise in the rate of storage tank density, particularly in grids with ~~a p-value less than~~ at a confidence level of p=0.05. This trend suggests that areas with active storage tank construction may contribute significantly to increased CH$_4$ emissions. Some grids exhibit high CH$_4$ emission increasing rates but low storage tank density increasing rates. This pattern suggests that while storage tank construction significantly contributes to CH$_4$ emissions, other sources related to energy

production, such as the extraction and transport of coal, oil, and natural gas, are also major contributors to $CH_4$ release. However, regarding the 92 typical ~~cities~~city regions with intensive storage tank distribution and construction, the impact of storage tank construction on $CH_4$ emission from energetic activities is largely statistically significant, especially in areas with a high rate of new storage tank construction. Therefore, it is necessary to propose effective measurements to mitigate $CH_4$ emissions from the continuously constructed storage tanks.

## 6. Discussion

### 6.1 Comparison with published Datasets

To the best of our knowledge, limited research has been published concerning remote sensing datasets on storage tanks. The dataset, NEPU–OWOD V1.0, is a recently proposed oil storage tank dataset featuring 1,192 oil storage tanks from 432 images of Google Earth. It covers the city of Daqing on a limited scale. However, the dataset lacks georeferenced information, hence the difficulty in supporting further research by governmental agencies and academic groups on various subjects such as air pollution control and energy consumption balance studies (Wang et al., 2021). ~~This is similar~~

Similar to the NEPU–OWOD V1.0 dataset, the Oil and Gas Tank Dataset is proposed (Rabbi et al., 2020), which comprises 760 image patches of size 512×512. The images are taken at a spatial resolution of 30 cm, and the annotations are boundary boxes rather than details on the exact shape. To assess the national energy demand, an oil storage tank dataset is released on the platform Kaggle (~~Heyer~~Airbusgeo, 2019). However, the images are collected from Google Earth without georeferenced information. Only 100 image patches of size 512×512 pixels are included in the dataset.

Publication of datasets on oil storage tanks is generally developed to improve automatic methods for the detection of storage tanks rather than further environmental analysis based on the combination and synthesis with datasets of other domains, such as air pollution products. Therefore, the proposed STD dataset is the first storage tank inventory that provides a detailed distribution of storage tanks of diverse ~~sizes~~footprints in 92 ~~cities~~city regions in China. Each storage tank in the dataset has undergone rigorous verification by six experts. Additionally, the dataset meticulously logs the construction year for each tank. This allows for an analysis of the temporal evolution of storage tank distribution and its combined effects with $CH_4$ emissions on the climate. Such insights pave the way for developing more effective energy management and climate change mitigation strategies, serving as a valuable resource for research in atmospheric science, environmental studies, and sustainable development.

### 6.2 Uncertainties, limitations, and implications

The Storage Tank Dataset (STD) we've compiled for 92 ~~cities~~city regions in China serves as a valuable tool for climate change research, despite certain limitations. The extraction process from high-resolution images is subject to inaccuracies due to shadows and the inherent limitations of representing three-dimensional tanks as two-

dimensional circles, potentially leading to slight positional errors (Figure 13A). Additionally, the variance in perspective between our collected high spatial resolution images and Google Earth historical images can cause deviations in visual refinement in the tanks' vectorized outlines (as shown in Figure 13B). To mitigate these issues, expert analysis is employed to ensure tank identification and location precision, referring to the collected high spatial resolution images.
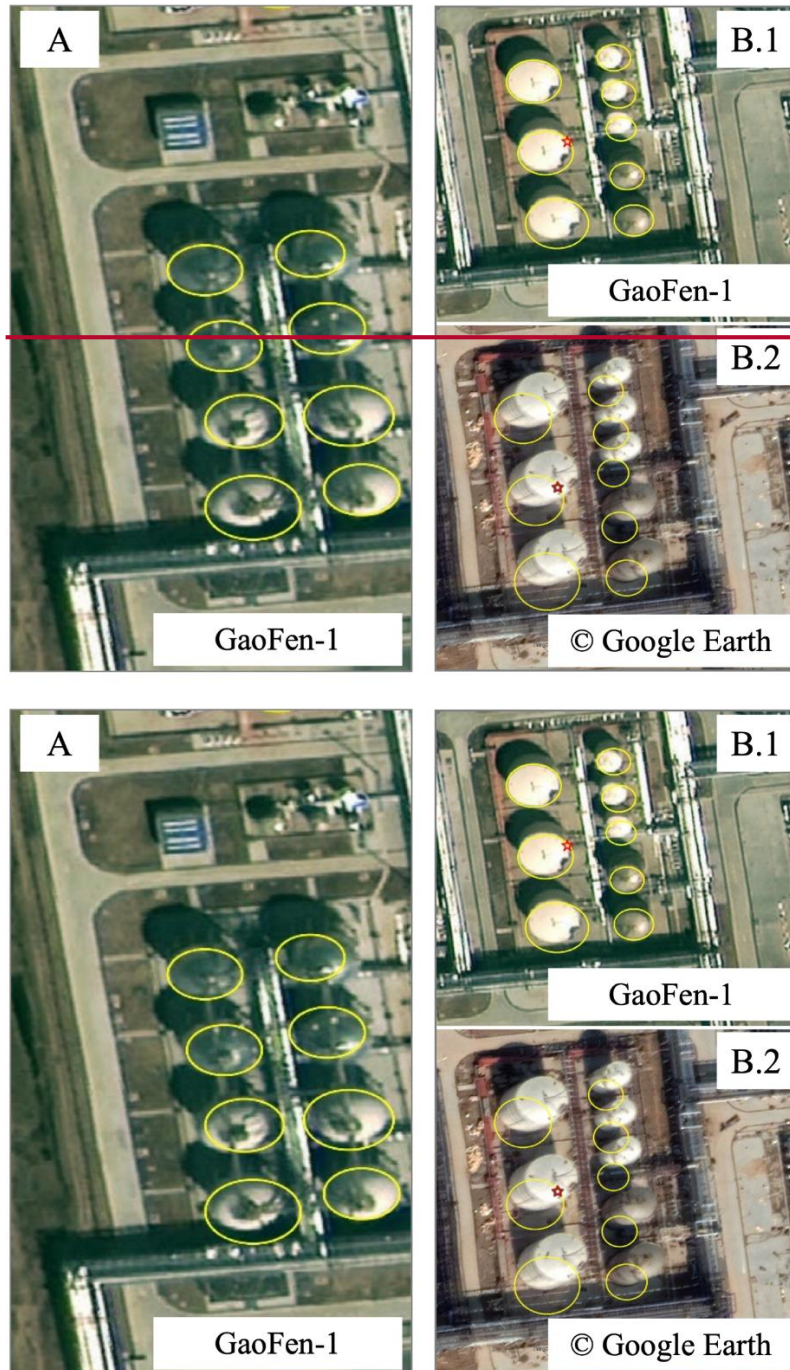


*Figure 13. Example cases of our proposed STD dataset: (A) cases with shifted circles due to cast by shadow; (B) cases with largely deviated circles in different images due to different viewing angles.*

The pioneering STD dataset encompasses georeferenced storage tank shapes for 92 key Chinese ~~cities~~city regions crafted from high-resolution images. For each storage tank, the corresponding construction year is assigned, referring to the high-resolution historical images of Google Earth. It's a versatile resource with spatial and temporal distribution patterns, not just for mapping $CH_4$ and other emissions but also for aiding the development of infrastructural strategies across various industries. However, the dataset currently lacks volumetric data due to the absence of height measurements for the tanks. Future enhancements aim to incorporate height data through advanced remote sensing technologies like SAR imagery, enriching the dataset with three-dimensional accuracy and providing a more comprehensive understanding of storage tank capacities.

## 7. Dataset availability

The STD dataset is publicly available as a repository at https://zenodo.org/records/10514151 (Chen et al., 2024). The dataset is provided in a shapefile, wherein a polygon with an area attribute in units of $m^2$ represents each storage tank, and two attributes of years, year_1 indicating the most recent year when a storage tank was absent (last year image without storage tank) and year_2 indicating the earliest year when it was first observed (first year image with storage tank). The inventory is intended to be used to further analyze the impact on $CH_4$ emissions, devise and implement more efficient energy management strategies. Moreover, our approach represents a powerful new source to improve automatic methods for storage tank extraction from high spatial resolution images, given that it represents a comprehensive and state-of-the-art inventory with tens of thousands of storage tanks georeferenced of 92 typical ~~cities~~city regions over China.

## 8. Conclusions

In support of $CH_4$ emission control to mitigate climate warming, the STD dataset is proposed by providing a meticulously georeferenced inventory of storage tanks larger than 500 $m^2$ across 92 key ~~cities~~city regions of China in years of 2000-2021. Leveraging a novel semantic segmentation framework, Res2-UnetA, and rigorous visual interpretation based on the collected high spatial resolution images, historical high spatial resolution images from Google Earth, and field survey, the dataset not only details the spatial distribution of large storage tanks but also includes their construction years. Based on the STD dataset, the spatial distribution pattern of the storage tanks of different ~~sizes~~footprints was analyzed in 92 ~~cities~~city regions. We also explored the impact of storage tank construction on $CH_4$ emission from energetic activities through 2005-2020. Compared with the published datasets for storage tanks, the STD dataset is the first inventory that compiles georeferenced storage tanks in 92 ~~cities~~city regions with detailed shape boundaries and construction years. In general, publicly available datasets on storage tanks typically cover only part of a city without georeferenced information and detailed shape boundaries. It is, therefore, difficult to objectively explore the extent and patterns of environmental impact and the energy management of the storage tanks at large scale. The STD dataset enables large-scale environmental

impact analysis of storage tanks and their correlation with $CH_4$ emissions. It demonstrates strong spatial consistency with $CH_4$ emissions in 92 typical Chinese ~~cities~~city regions, highlighting the substantial increase in $CH_4$ emissions due to storage tank construction. The storage tank dataset STD can contribute significantly to supporting energy management strategies and sustainability development studies while giving direct support to academic research and government agencies.

## Author contributions

FC and LW designed the study and conducted the experiments. YW, HZ, NW, PM and BY compiled the dataset. BY wrote the manuscript.

## Competing interests

The authors declare that they have no conflicts of interest.

## Financial support

## References

Amann, M., Bertok, I., Borken-Kleefeld, J., Cofala, J., Heyes, C., Höglund-Isaksson, L., Klimont, Z., Nguyen, B., Posch, M., and Rafaj, P.: Cost-effective control of air quality and greenhouse gases in Europe: Modeling and policy applications, Environmental Modelling & Software, 26, 1489-1501, 2011.

Airbusgeo: Airbus oil storage detection, dataset website: https://www.kaggle.com/datasets/airbusgeo/airbus-oil-storage-detection-dataset, 2019.

Badrinarayanan, V., Kendall, A., and Cipolla, R.: Segnet: A deep convolutional encoder-decoder architecture for image segmentation, IEEE ~~transactions~~Transactions on ~~pattern analysis~~Pattern Analysis and ~~machine intelligence~~Machine Intelligence, 39, 2481-2495, 2017.

Chen, F., Wang, N., Yu, B., and Wang, L.: Res2-Unet, a new deep architecture for building detection from high spatial resolution images, IEEE Journal of Selected Topics in Applied Earth Observations and Remote Sensing, 15, 1494-1501, 2022.

Chen, F., Wang, J., Li, B., Yang, A., and Zhang, M.: Spatial variability in melting on Himalayan debris-covered glaciers from 2000 to 2013, Remote Sensing of Environment, 291, 113560, ~~https://doi.org/10.1016/j.rse.2023.113560, 2023.~~2023.

Chen, F., Wang, L., Wang, Y., Zhang, H., Wang, N., Ma, P., and Yu, B. (2024). Retrieval of

dominant methane (CH4) emission sources, the first high resolution(1-2m) dataset of storage tank in China in 2021, Zenodo [data set], https://zenodo.org/records/10514151, 2024

Chen, L.-C., Papandreou, G., Schroff, F., and Adam, H.: Rethinking atrous convolution for semantic image segmentation, arXiv preprint arXiv:1706.05587, 2017a.

Chen, L.-C., Papandreou, G., Kokkinos, I., Murphy, K., and Yuille, A. L.: Deeplab: Semantic image segmentation with deep convolutional nets, atrous convolution, and fully connected crfs, IEEE ~~transactions~~Transactions on ~~pattern analysis~~Pattern Analysis and ~~machine intelligence~~Machine Intelligence, 40, 834-848, 2017b.

Crippa, M., Oreggioni, G., Guizzardi, D., Muntean, M., Schaaf, E., Lo Vullo, E., Solazzo, E., Monforti-Ferrario, F., Olivier, J. G., and Vignati, E.: Fossil CO2 and GHG emissions of all world countries, Publication Office of the European Union: Luxemburg, 2019.

Ding, T., Ning, Y., and Zhang, Y.: Estimation of greenhouse gas emissions in China 1990–2013, Greenhouse Gases: Science and Technology, 7, 1097-1115, 2017.

Fan, L., Chen, X., Wan, Y., and Dai, Y.: Comparative Analysis of Remote Sensing Storage Tank Detection Methods Based on Deep Learning, Remote Sensing, 15, 2460, 2023.

Gao, S.-H., Cheng, M.-M., Zhao, K., Zhang, X.-Y., Yang, M.-H., and Torr, P.: Res2net: A new multi-scale backbone architecture, IEEE ~~transactions~~Transactions on ~~pattern analysis~~Pattern Analysis and ~~machine intelligence~~Machine Intelligence, 43, 652-662, ~~2019.~~

~~Heyer, K.: Airbus oil storage detection,~~ 2019.

Hoesly, R. M., Smith, S. J., Feng, L., Klimont, Z., Janssens-Maenhout, G., Pitkanen, T., Seibert, J. J., Vu, L., Andres, R. J., and Bolt, R. M.: Historical (1750–2014) anthropogenic emissions of reactive gases and aerosols from the Community Emissions Data System (CEDS), Geoscientific Model Development, 11, 369-408, 2018.

Hou, B., Ren, Z., Zhao, W., Wu, Q., and Jiao, L.: Object detection in high-resolution panchromatic images using deep models and spatial template matching, IEEE Transactions on Geoscience and Remote Sensing, 58, 956-970, 2019.

Hou, D., Miao, Z., Xing, H., and Wu, H.: Two novel benchmark datasets from ArcGIS and bing world imagery for remote sensing image retrieval, International Journal of Remote Sensing, 42, 240-258, 2021.

Im, S., Mostafa, A., Lim, K.-H., Kim, I., and Kim, D.-H.: Automatic temperature rise in the manure storage tank increases methane emissions: Worth to cool down!, Science of The Total Environment, 823, 153533, 2022.

Johnson, D., Clark, N., Heltzel, R., Darzi, M., Footer, T. L., Herndon, S., and Thoma, E. D.: Methane emissions from oil and gas production sites and their storage tanks in West Virginia, Atmospheric Environment: X, 16, 100193, 2022.

Karra, K., Kontgis, C., Statman-Weil, Z., Mazzariello, J. C., Mathis, M., and Brumby, S. P.: Global land use/land cover with Sentinel 2 and deep learning, ~~2021~~ IEEE ~~international geoscience~~International Geoscience and ~~remote sensing symposium~~Remote Sensing Symposium

IGARSS, 4704-4707, 2021

Kirschke, S., Bousquet, P., Ciais, P., Saunois, M., Canadell, J. G., Dlugokencky, E. J., Bergamaschi, P., Bergmann, D., Blake, D. R., Bruhwiler, L., Cameron-Smith, P., Castaldi, S., Chevallier, F., Feng, L., Fraser, A., Heimann, M., Hodson, E. L., Houweling, S., Josse, B., Fraser, P. J., Krummel, P. B., Lamarque, J.-F., Langenfelds, R. L., Le Quéré, C., Naik, V., O'Doherty, S., Palmer, P. I., Pison, I., Plummer, D., Poulter, B., Prinn, R. G., Rigby, M., Ringeval, B., Santini, M., Schmidt, M., Shindell, D. T., Simpson, I. J., Spahni, R., Steele, L. P., Strode, S. A., Sudo, K., Szopa, S., van der Werf, G. R., Voulgarakis, A., van Weele, M., Weiss, R. F., Williams, J. E., and Zeng, G.: Three decades of global methane sources and sinks, Nature Geoscience, 6, 813-823, 10.1038/ngeo1955, 2013.

Kurokawa, J., Ohara, T., Morikawa, T., Hanayama, S., Janssens-Maenhout, G., Fukui, T., Kawashima, K., and Akimoto, H.: Emissions of air pollutants and greenhouse gases over Asian regions during 2000–2008: Regional Emission inventory in ASiaAsia (REAS) version 2, Atmospheric Chemistry and Physics, 13, 11019-11058, 2013.

Lane, K.: IEA Energy Efficiency 2018 and World Energy Outlook 2018, Brussels, November, 27, 2018.

Lin, X., Zhang, W., Crippa, M., Peng, S., Han, P., Zeng, N., Yu, L., and Wang, G.: A comparative study of anthropogenic CH4 emissions over China based on the ensembles of bottom-up inventories, Earth Syst. Sci.System Science Data, 13, 1073-1088, 10.5194/essd-13-1073-2021, 2021.

Long, J., Shelhamer, E., and Darrell, T.: Fully convolutional networks for semantic segmentation, Proceedings of the IEEE conferenceConference on computer visionComputer Vision and pattern recognitionPattern Recognition, 3431-3440, 2015

Majumder, A., He, Z., Towles, H., and Welch, G.: Achieving color uniformity across multi-projector displays, Proceedings Visualization 2000. VIS 2000 (Cat. No. 00CH37145), 117-124, 1-8, 2010

Montzka, S. A., Dlugokencky, E. J., and Butler, J. H.: Non-CO2 greenhouse gases and climate change, Nature, 476, 43-50, 2011.

O'DUDA, R.: Use of Hough transformation to detect lines and curves in picture, CACMCommunications of the ACM, 15,(1), 11-15, 1972.

Peng, S., Piao, S., Bousquet, P., Ciais, P., Li, B., Lin, X., Tao, S., Wang, Z., Zhang, Y., and Zhou, F.: Inventory of anthropogenic methane emissions in mainland China from 1980 to 2010, Atmospheric Chemistry and Physics, 16, 14545-14562, 2016.

Rabbi, J., Ray, N., Schubert, M., Chowdhury, S., and Chao, D.: Small-Object Detection in Remote Sensing Images with End-to-End Edge-Enhanced GAN and Object Detector Network, 10.3390/rs12091432, Remote Sensing, 12, 1432, 2020.

Ronneberger, O., Fischer, P., and Brox, T.: U-net: Convolutional networks for biomedical image segmentation, Medical Image Computing and Computer-Assisted Intervention–MICCAI 2015: 18th International Conference, Munich, Germany, October 5-9, 2015, Proceedings, Part III 18, 234-241,, 234-241, 2015

Sahu, V. and Sahu, D.: Image fusion using wavelet transform: a review, Global Journal of Computer

Science and Technology, ~~Global Journals Inc.(USA), ISSN, 975, 4172~~Corpus ID 35285493, 2014.

Shen, D.: Image registration by local histogram matching, Pattern Recognition, 40, 1161-1172, 2007.

Stocker, T.: Climate change 2013~~:~~ - the physical science basis~~:~~, Working Group I contribution to the Fifth assessment report of the Intergovernmental Panel on Climate Change, Cambridge university ~~press2014~~press, 2014.

Venter, Z. S., Barton, D. N., Chakraborty, T., Simensen, T., and Singh, G.: Global 10 m Land Use Land Cover Datasets: A Comparison of Dynamic World, World Cover and Esri Land Cover, Remote Sensing, 14, 4101, 2022.

Vermote, E. F., Tanré, D., Deuze, J. L., Herman, M., and Morcette, J.-J.: Second simulation of the satellite signal in the solar spectrum, 6S: An overview, IEEE ~~transactions~~Transactions on ~~geoscience~~Geoscience and ~~remote sensing~~Remote Sensing, 35, 675-686, 1997.

Wang, H., Sun, S., Nie, L., Zhang, Z., Li, W., and Hao, Z.: A review of whole-process control of industrial volatile organic compounds in China, Journal of Environmental Sciences, 123, 127-139, 2022.

Wang, Z., Bai, L., Song, G., Zhang, J., Tao, J., Mulvenna, M. D., Bond, R. R., and Chen, L.: An Oil Well Dataset Derived from Satellite-Based Remote Sensing, ~~10.3390/rs13061132,~~ 13, 1132, 2021.

Wu, Q., Zhang, B., Xu, C., Zhang, H., and Wang, C.: Dense Oil Tank Detection and Classification via YOLOX-TR Network in Large-Scale SAR Images, Remote Sensing, 14, 3246, 2022.

Xia, X., Liang, H., RongFeng, Y., and Kun, Y.: Oil tank extraction in high-resolution remote sensing images based on deep learning, 2018 26th International Conference on Geoinformatics, 1-6, 2018

Yang, L., Meng, X., and Zhang, X.: SRTM DEM and its application advances, International Journal of Remote Sensing, 32, 3875-3896, 2011.

Yu, B., Chen, F., Wang, N., Wang, L., and Guo, H.: Assessing changes in nighttime lighting in the aftermath of the Turkey-Syria earthquake using SDGSAT-1 satellite data, The Innovation, 4, 100419, 2023a.

Yu, B., Xu, C., Chen, F., Wang, N., and Wang, L.: HADeenNet: A hierarchical-attention multi-scale deconvolution network for landslide detection, International Journal of Applied Earth Observation and Geoinformation, 111, 102853, 2022a.

Yu, B., Yang, A., Chen, F., Wang, N., and Wang, L.: SNNFD, spiking neural segmentation network in frequency domain using high spatial resolution images for building extraction, International Journal of Applied Earth Observation and Geoinformation, 112, 102930, 2022b.

Yu, B., Chen, F., Ye, C., Li, Z., Dong, Y., Wang, N., and Wang, L.: Temporal expansion of the nighttime light images of SDGSAT-1 satellite in illuminating ground object extraction by joint observation of NPP-VIIRS and sentinel-2A images, Remote Sensing of Environment, 295, 113691, ~~https://doi.org/10.1016/j.rse.2023.113691, 2023b.~~2023b.

Yu, B., Chen, F., Wang, Y., Wang, N., Yang, X., Ma, P., Zhou, C., and Zhang, Y.: Res2-Unet+, a Practical Oil Tank Detection Network for Large-Scale High Spatial Resolution Images, Remote

811    Sensing, 13, 4740, 2021.

812    Yuen, H., Princen, J., Illingworth, J., and Kittler, J.: Comparative study of Hough transform methods
813    for circle finding, Image and ~~vision computing~~Vision Computing, 8, 71-77, 1990.

814    Zalpour, M., Akbarizadeh, G., and Alaei-Sheini, N.: A new approach for oil tank detection using
815    deep learning features with control false alarm rate in high-resolution satellite imagery, International
816    Journal of Remote Sensing, 41, 2239-2262, ~~10.1080/01431161.2019.1685720,~~ 2020.

817    Zhang, L. and Liu, C.: Oil tank extraction based on joint-spatial saliency analysis for multiple SAR
818    images, IEEE Geoscience and Remote Sensing Letters, 17, 998-1002, 2019.

819    Zhang, Z., Hu, S., and Jing, Y.: 2060 China Carbon Neutral-Fossil Energy to Fossil Resource Age,
820    ~~Mod. Chem~~Modern Chemistry, 41, 1-5, 2021.

821    Zhao, H., Shi, J., Qi, X., Wang, X., and Jia, J.: Pyramid scene parsing network, Proceedings of the
822    IEEE ~~conference~~Conference on ~~computer vision~~Computer Vision and ~~pattern recognition, 2881-~~
823    ~~2890~~Pattern Recognition, 6230-6239, 2017